scientific reports

Check for updates

OPEN

Mott–Hubbard insulating state for the layered van der Waals $FePX_3$ (X: S, Se) as revealed by NEXAFS and resonant photoelectron spectroscopy

Yichen Jin[1], Mouhui Yan[1], Tomislav Kremer[2], Elena Voloshina[1,2,3]✉ & Yuriy Dedkov[1,2,3]✉

A broad family of the nowadays studied low-dimensional systems, including 2D materials, demonstrate many fascinating properties, which however depend on the atomic composition as well as on the system dimensionality. Therefore, the studies of the electronic correlation effects in the new 2D materials is of paramount importance for the understanding of their transport, optical and catalytic properties. Here, by means of electron spectroscopy methods in combination with density functional theory calculations we investigate the electronic structure of a new layered van der Waals $FePX_3$ (X: S, Se) materials. Using systematic resonant photoelectron spectroscopy studies we observed strong resonant behavior for the peaks associated with the $3d^{n-1}$ final state at low binding energies for these materials. Such observations clearly assign $FePX_3$ to the class of Mott–Hubbard type insulators for which the top of the valence band is formed by the hybrid Fe-S/Se electronic states. These observations are important for the deep understanding of this new class of materials and draw perspectives for their further applications in different application areas, like (opto)spintronics and catalysis.

The large part of research in the rapidly developing areas of science, like nanotechnology and catalysis, is devoted to the search of new materials and to the studies of their electronic structure[1,2]. Such experimental and theoretical studies help to make a link between fundamental knowledge and the possible applications. Here, e. g., layered materials, which are in the focus of the present-day intensive research, give a big hope on further development of new systems with unique electronic and transport properties, which can bring new functionalities in (nano) electronics, materials synthesis, (nano)catalysis, etc.[3–5]. The initial and following experiments on graphene, the first pure 2D material which initiated the present boom in this area, demonstrated the large perspectives of this material in the application in different areas ranging from protective layers and coatings, gas sensors to photosensors and touchscreens[6–9]. However, the further progress in the implementation of graphene in the modern serial production is connected with many factors[10,11] and among them is the absence of the energy gap in the carriers' spectrum. This fact requires further modifications of graphene (chemical or structural), which in most cases lead to the uncontrollable variations of the electronic properties of the 2D layer or system[12–15]. The search of the new 2D materials with a natural band gap in the spectrum and the progress in their studies bring several di- and tri-atomic materials which can be considered as perspective in future applications[16–20].

Among the layered materials which recently attract much attention are transition metal trichalcogenides (TMT) with the formula MPX_3 (M is the transition metal cation and X is S or Se) with large van der Waals gap between single layers[18,20,21]. Because the ionic-like interaction between M^{2+} and $(P_2X_6)^{4-}$ units in the single layer, these compounds in almost all cases are antiferromagnetic (AFM) wide-gap semiconductors with the energy gap ranging between 1.3 eV and 3.5 eV[19,21–23]. Due to these facts and because of the variety of the M-X combinations, these materials were proposed and tested for different applications, like photocatalytic water splitting[18,22,24], spintronic applications[25,26], low-dimensional magnetic devices[27–29], and many others[20]. Here, among other MPX_3,

[1]Department of Physics, Shanghai University, 99 Shangda Road, Shanghai 200444, People's Republic of China. [2]Institut für Chemie und Biochemie, Freie Universität Berlin, 14195 Berlin, Germany. [3]Centre of Excellence ENSEMBLE3 Sp. z o. o., Wolczynska Str. 133, 01-919 Warsaw, Poland. ✉email: elena.voloshina@icloud.com; yuriy.dedkov@icloud.com

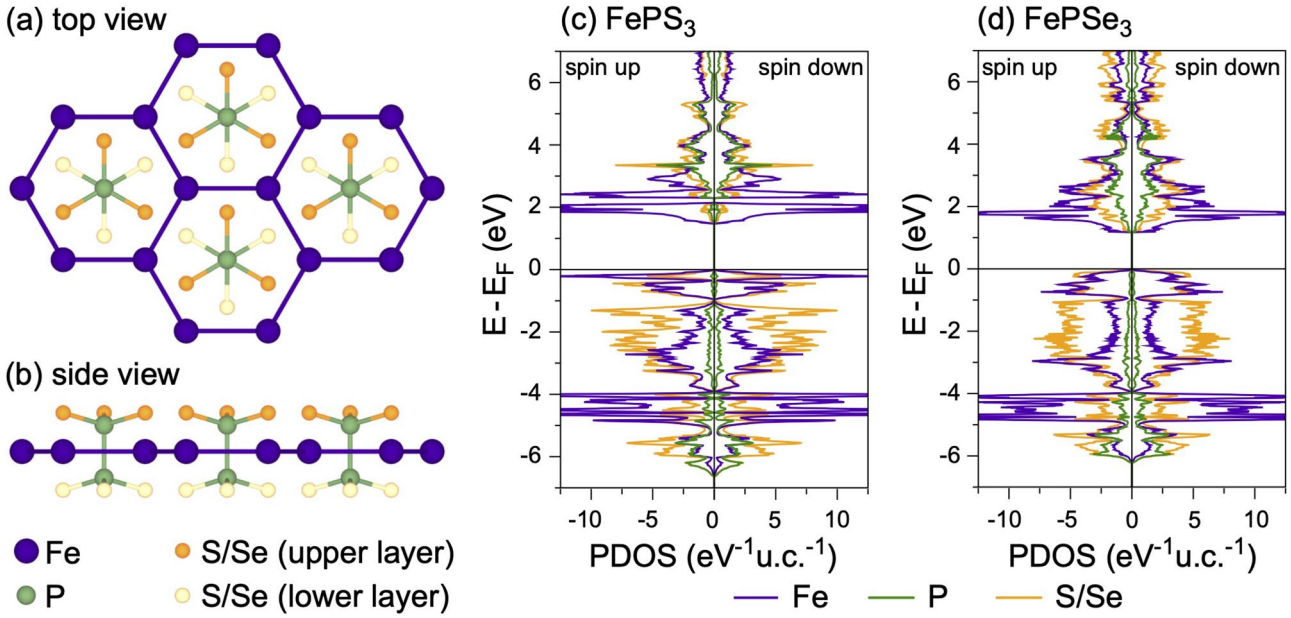

Figure 1. Top (**a**) and side (**b**) views of the crystallographic structure of the $FePX_3$ (X: S or Se) single layer. Atom-projected partial DOS for bulk $FePS_3$ (**c**) and $FePSe_3$ (**d**) in the AFM ground state. Images are created using CrystalMaker X (Version: 10.7.0), http://www.crystalmaker.com and Igor Pro (Version 9), https://www.wavemetrics.com.

the $FePX_3$ TMTs have gained increased interest because of the recent studies of (1) magnetic properties with the observations of the giant optical linear dichroism[30,31] and (2) photoelectrochemical water splitting where best fit of the band gap of $FePX_3$ to the redox potentials of water splitting at $pH = 0$ and $pH = 7$ was found[22,32]. Here, Fe^{2+} cations can be considered as isoelectron to Ru-ion in Ru-based complexes, which are found to be very efficient water oxidation agents[33–35].

Despite the widely discussed perspectives on the application of TMTs in different areas, surprisingly, not many works are devoted to the studies of the electronic structure of TMTs compounds, in particular of $FePX_3$. In most cases, only theoretical analysis of the electronic and magnetic structures is presented. However, such basic studies of the electronic structure using different spectroscopic methods, can give a direct insight in the understanding of properties which can be directly connected with the applied-oriented research. Recently we performed intensive electronic structure studies of the layered $NiPS_3$ compound using near-edge x-ray absorption fine structure spectroscopy (NEXAFS) and resonant photoelectron spectroscopy (ResPES) which clearly identify this materials as a charge-transfer insulator[36]. In the present work, we perform systematic combined experimental and theoretical studies of a layered $FePX_3$ (X: S, Se) family of TMTs. Our ex situ and in situ structural studies demonstrate very high bulk and surface quality of the studied materials permitting accurate experiments using surface-sensitive electron spectroscopy techniques, NEXAFS and ResPES. These methods, being element and orbital selective, allow in combination with density-functional theory (DFT) calculations to obtain the detailed information about the character of electronic states in the valence and conduction bands of $FePX_3$. The obtained results allow us to assign the layered $FePX_3$ materials to the Mott–Hubbard type insulator according to the Zaanen–Sawatzky–Allen scheme, opposite to the charge-transfer insulator ($NiPS_3$).

Results and discussion

DFT. The crystallographic structure of a $FePX_3$ monolayer can be considered as a layer of MoS_2 where one third of metal atoms is replaced by the P–P dimers which are perpendicular to the TMT layer and form the ethane-like structure with X-atoms (Fig. 1a,b), thus Fe-cations form the graphene-like honeycomb structure. The monolayers of $FePX_3$ stack in the $C2/m$ and $R\bar{3}$ space groups with the van der Waals gap of 3.32 Å and 3.26 Å between neighboring chalcogen layers for X = S and X = Se, respectively (see Fig. S1, Table S1 and corresponding structural files in the Supplementary Information). Both 3D $FePX_3$ compounds are AFM in the ground states with the distance between layers $c' = 6.537(6.621)$ Å for X = S (Se), respectively. The mixing character of interaction (ionic and covalent) in the structural unit of $FePX_3$ leads to the specific distribution of valence band states in the calculated density of states (DOS). As can be seen, both $FePX_3$ compounds are wide band gap semiconductors with an energy gap of 1.48 eV and 1.17 eV for X = S and X = Se, respectively (Fig. 1c,d). The space and energy overlap between Fe 3*d* and S/Se,*sp* leads to the formation of the respective hybrid bands in the whole energy range of DOS. The top of the valence band of $FePX_3$ is formed by the hybrid Fe-S/Se states with the significant contribution of the Fe 3*d* partial DOS. The same is also valid for the bottom of the conduction band. At the same time the less localized character of the electronic states, and particularly of the Fe 3*d* states, can be noted for $FePSe_3$.

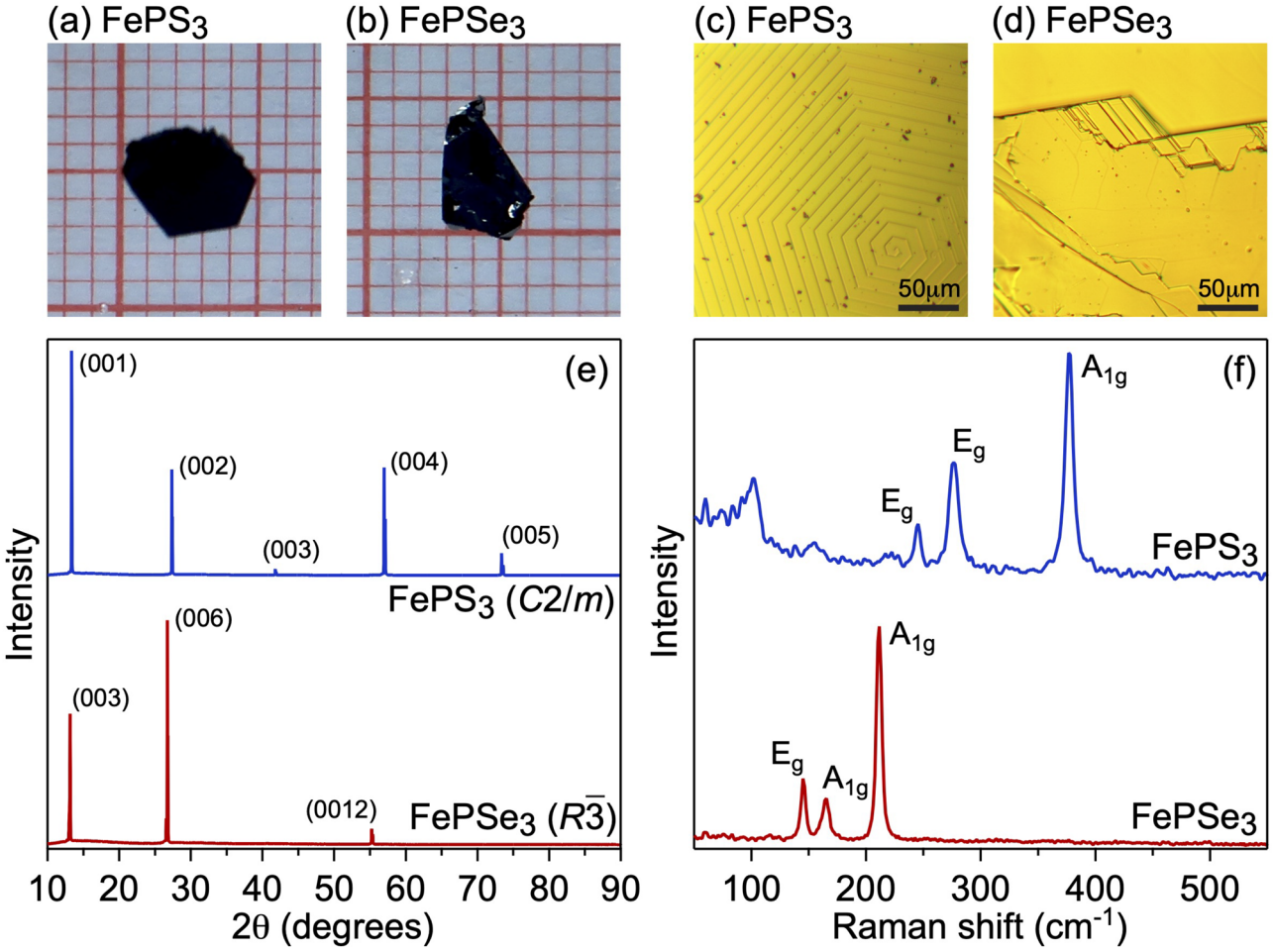

Figure 2. Characterization of $FePX_3$ crystals: (**a**,**b**) photos, (**c**,**d**) optical microscopy images, (**e**) XRD patterns and (**f**) Raman spectra measured at room temperature for bulk samples. Images are created using Igor Pro (Version 9), https://www.wavemetrics.com.

The presented distribution of the electronic states in DOS of $FePX_3$ is different from those for isostructural $NiPS_3$ and similar to the states distribution for isostructural $MnPX_3$ (although not so energy localized for the metal-projected partial DOS)[23,36,37]. According to the Zaanen–Sawatzky–Allen scheme[38], the electronic structure of oxides and sulphides can be described with two parameters, the $d-d$ correlation energy (U_{dd}) and charge transfer energy between d-states of the metal and p-states of the ligand (Δ). Taking into account this scheme, the later compounds can be assigned to two limit cases of Mott–Hubbard type insulator ($U_{dd} < \Delta$) for $MnPX_3$ (Mn^{2+} $3d^5$) and charge-transfer type insulator ($U_{dd} > \Delta$) for $NiPS_3$ (Ni^{2+} $3d^8$). In case of $FePX_3$ the obtained values of $U_{dd} = 3$ eV and $\Delta \approx 6$ eV (Δ is taken as a difference between centres of gravity for the occupied and unoccupied ligand partial DOS) place these materials to the case of Mott–Hubbard type insulator.

Characterization. Figures 2 and S2 summarize the experimental results on the bulk characterization of the $FePX_3$ crystals studied in the present work. Well-ordered single crystalline samples with the linear sizes up to several-mm clearly demonstrate layered structure in optical images with angles between crystalline edges either 60° or 120° confirming hexagonal atomic arrangement in a single $FePX_3$ layer (Fig. 2a–d). In the XRD plots of the $FePX_3$ layered samples there are only (00l) preferred orientation peaks which confirm high bulk quality and the respective space symmetry groups of $FePX_3$ crystals (Fig. 2e)[21,39]. The interlayer distances for $FePS_3$ and $FePSe_3$ extracted from the TEM data are 6.45 Å and 6.64 Å, respectively (Fig. S2), which are in very good agreement with previously published structural data for these compounds[21] and with our present theoretical results (see above). Raman spectroscopy characterization also confirm a high quality of the studied $FePX_3$ crystals where observed peaks can be assigned to the corresponding vibrations involving metal atoms (broad bands at 101 cm^{-1} for $FePS_3$ and 117 cm^{-1} for $FePSe_3$) and the other come from the vibrations of the $[P_2X_6]$ unit with a D_{3d} symmetry group ($FePS_3$: 155 cm^{-1}, 245 cm^{-1}, 276 cm^{-1}, 376 cm^{-1}; $FePSe_3$: 145 cm^{-1}, 165 cm^{-1}, 211.5 cm^{-1})[21,32,40,41].

Freshly cleaved surfaces of $FePX_3$ crystals were used for SEM/EDX measurements (Fig. 3a,b). The obtained SEM images also confirm the high crystallographic quality of the obtained surfaces with the terraces width of several hundreds μm. The measured EDX maps shown below the respective SEM images confirm the uniform distribution of elements and the stoichiometry of the studied samples (Fig. 3a,b and Fig. S3). After characterization, freshly cleaved samples were introduced in UHV and annealed at 350 °C. Following this procedure, the

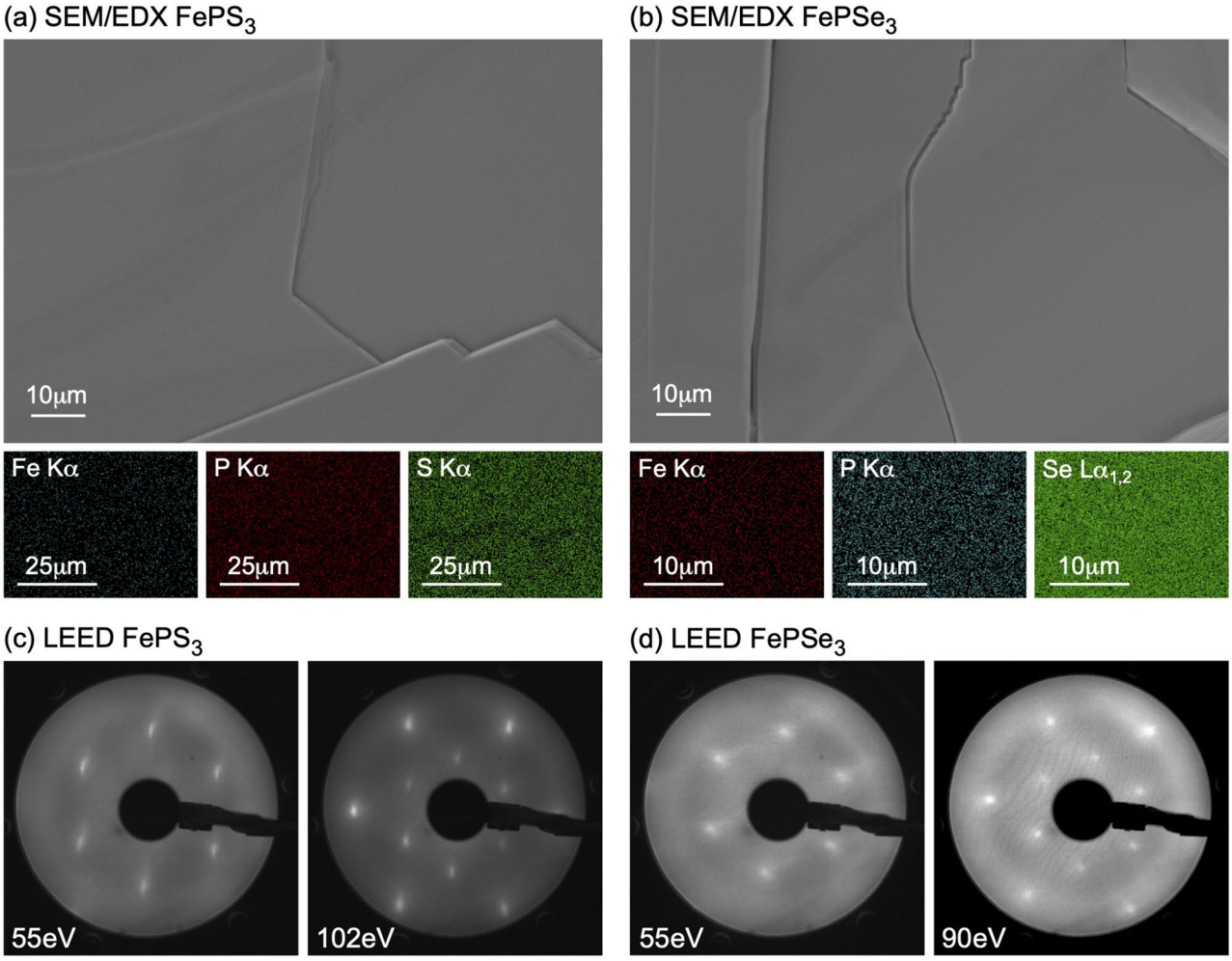

Figure 3. (**a**,**b**) SEM and the respective EDX maps collected at the primary electron beam energy of 15 keV for $FePS_3$ and $FePSe_3$, respectively. (**c**,**d**) Set of LEED images collected for freshly cleaved and annealed $FePS_3$ and $FePSe_3$ samples, respectively. Energies for the primary electron beam are marked in every image. Images are compiled using Adobe Illustrator 2022 (Version 26.0.2), https://www.adobe.com.

measured LEED images (Fig. 3c,d) show clear hexagonal diffraction patterns indicating the long-range structural ordering of the $FePX_3$(001) surfaces without structural defects and surface adsorbates. The slightly diffuse diffraction spots observed at low primary electron beam energies can be assigned to the residual charging effects for the wide-band semiconducting $FePX_3$ and the less sharp picture in case of $FePSe_3$(001) is due to the less structural ordering of the $FePSe_3$ samples as can be seen from optical and SEM images.

XPS and NEXAFS. Figure 4 shows compilation of the XPS and NEXAFS spectra of freshly-cleaved and UHV-annealed $FePX_3$ crystals collected for the representative core-level emission lines and at the respective absorption edges (the Se $M_{4,5}$ spectrum for $FePSe_3$ is not shown). In these compounds Fe^{2+} cations are octahedrally coordinated with S-ions. Therefore Fe 2*p* XPS (Fig. 4a) and Fe $L_{2,3}$ NEXAFS spectra (Fig. 4e) are very similar to those for FeO (Fe^{2+}), which is assigned to the class of Mott–Hubbard insulator[42–46]. Particularly it is visible for the photoemission satellite structure for the respective XPS emission line. The extracted energy difference between Fe $2p_{3/2}$ main line and the satellite is 4.5 eV and 4.95 eV for $FePS_3$ and $FePSe_3$, respectively. These values can be compared to the corresponding ones of 5.5 eV for FeO (Fe^{2+}) and 8.0 eV for Fe_2O_3 (Fe^{3+})[42,43]. The interesting feature of the Fe 2*p* XPS spectra for $FePX_3$ materials is the observation of the "*metallic*-like" feature located at 708.5 eV (721.9 eV) of binding energy for Fe $2p_{3/2}$ (Fe $2p_{1/2}$) spin-orbit split components (it is mostly pronounced for $FePSe_3$) and which was not observed for the previously studied isostructural $NiPS_3$[36]. The nature of this spectral feature is not fully clear and could be a subject of further studies.

The same consideration is also valid for the description of the Fe $L_{2,3}$ NEXAFS spectra of $FePX_3$ (the respective NEXAFS spectra for both compounds are almost identical) (Fig. 4e). Generally, in case of FeO and $FePX_3$ for the Fe^{2+} cation in the octahedral ligand field the Fe $L_{2,3}$ NEXAFS spectra are very similar to each other (cf. Fig. 4e and data in Refs.[44,45,47]) and different from the one for Fe_3O_4 (Fe^{2+}/Fe^{3+}) and Fe_2O_3 (Fe^{3+}). According to the crystal-field approach, the NEXAFS spectra of FeO were simulated using the octahedral crystal field splitting parameter $10Dq = 0.4$ eV between t_{2g} and e_g orbitals[44]. In the present modelling using crystal-filed approach we used slightly smaller value of $10Dq = 0.3$ eV due to the weaker ligand field of the S/Se ions and the good

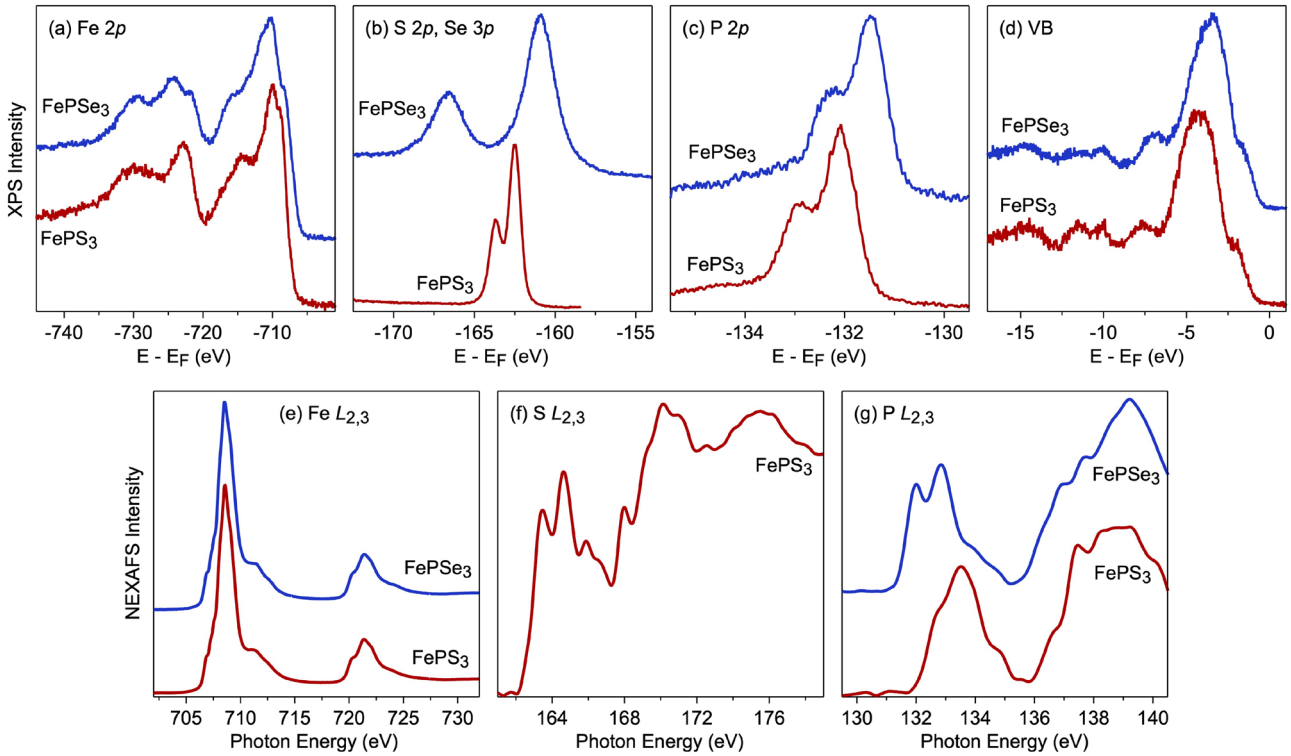

Figure 4. XPS spectra of $FePX_3$ collected at $h\nu = 1000$ eV: (**a**) Fe 2*p*, (**b**) S 2*p* and Se 3*p*, (**c**) P 2*p*, and (**d**) valence band region. NEXAFS spectra of $FePX_3$ collected in the TEY mode: (**e**) Fe $L_{2,3}$, (**f**) S $L_{2,3}$, and (**g**) P $L_{2,3}$. Images are created using Igor Pro (Version 9), https://www.wavemetrics.com.

agreement with the experimental spectra is found for the values of $U_{dd} = 3$ eV and $\Delta = 6$ eV (Fig. S4) confirming the description of $FePX_3$ as a Mott–Hubbard type insulator.

The S 2*p*/Se 3*p* and P 2*p* XPS spectra of $FePX_3$ show clear spin-orbit split structure (Fig. 4b,c). The difference in the binding energy of the P 2*p* line between $FePS_3$ and $FePSe_3$ of ≈ 0.6 eV is due to the slightly smaller electronegativity of Se compared to S and to the smaller value of the valence band maximum (VBM) position extracted from the valence band spectra – $E_{VBM} - E_F = -0.78$ eV for $FePS_3$ vs. $E_{VBM} - E_F = -0.45$ eV for $FePSe_3$ (because of the different band gaps of two materials; see above) (Fig. 4d). The respective S $L_{2,3}$ and P $L_{2,3}$ NEXAFS spectra of $FePX_3$ (Fig. 4f,g) correspond to the electronic transitions from the S/P spin-orbit split $2p_{3/2,1/2}$ level onto the unoccupied *d* and *s* states in the conduction band. As was stated in Ref.[36], the interpretation of these spectra is not a trivial task and, as was already discussed, the structure in the S $L_{2,3}$ and in the P $L_{2,3}$ spectra at $\approx 161 - 167$ eV and ≈ 131–136 eV of photon energy, respectively, can be assigned to the electron transitions into the first unoccupied hybrid 3*s*-like antibonding state formed by S/Se and P[36,47–49]. Additional high photon energy structure in the NEXAFS spectra can be assigned to the so-called "echo" or shadow effect of the spin-orbit split features due to multiple scattering or to electron transitions to a mixed-valence band states[48].

ResPES at the Fe $L_{2,3}$ edge. The method of the resonant photoelectron spectroscopy for electronic correlated systems is a unique tool allowing to clearly assign the studied objects to one of the classes of insulating systems which are classified according to the discussed Zaanen–Sawatzky–Allen scheme[38]. Figure 5 presents the compilation of the respective results for $FePX_3$ crystals: (a) reference Fe $L_{2,3}$ NEXAFS spectra and (b,c) a series of photoelectron emission spectra collected at the particular photon energies marked by the vertical lines in panel (a). For the ResPES measurements of 3*d*-derived valence band states at the Fe $L_{2,3}$ absorption edge on $FePX_3$, the photoemission intensity is a result of the interference of two photoemission channels[50–52]: (i) a direct photoelectron emission from the valence band states $2p^6 3d^n + h\nu \rightarrow 2p^6 3d^{n-1} + e$ and (ii) a photoabsorption process followed by a participator Coster-Kronig decay $2p^6 3d^n + h\nu \rightarrow 2p^5 3d^{n+1} \rightarrow 2p^6 3d^{n-1} + e$, where final states for these photoelectron emission channels are identical. The interference between these two photoemission channels leads to the Fano-type resonance for the states with the $3d^{n-1}$ final-state character.

For transition metal chalcogenides (oxides or sulfides) it was shown[53–57] that in case of the charge-transfer insulator state with $U_{dd} > \Delta$ (NiO, NiS, or NiS_2) the core-level or valence band XPS spectra consist of the intense low binding energy peak which is formed by the mixing of the $3d^n\underline{L}$ and $3d^n\underline{Z}$ final states ($\underline{L}$ and $\underline{Z}$ are a ligand hole and Zhang-Rice doublet bound states, respectively), and the high binding energy peak of the lower intensity is connected with the $3d^{n-1}$ final state. In case of the Mott–Hubbard type insulator state when $U_{dd} < \Delta$ (MnO or FeO) the situation is reversed and the intense low binding energy peak originates mainly from the $3d^{n-1}$ final state with the low intensity satellite $3d^n\underline{L}$ structure at large binding energies. Therefore, taking into account the fact that for the $2p \rightarrow 3d$ resonant photoemission the Coster-Kronig decay channel (marked as (ii)) dominates in the photoemission spectra[50,51], these measurements can give a position of the $3d^{n-1}$ peak relative to the one

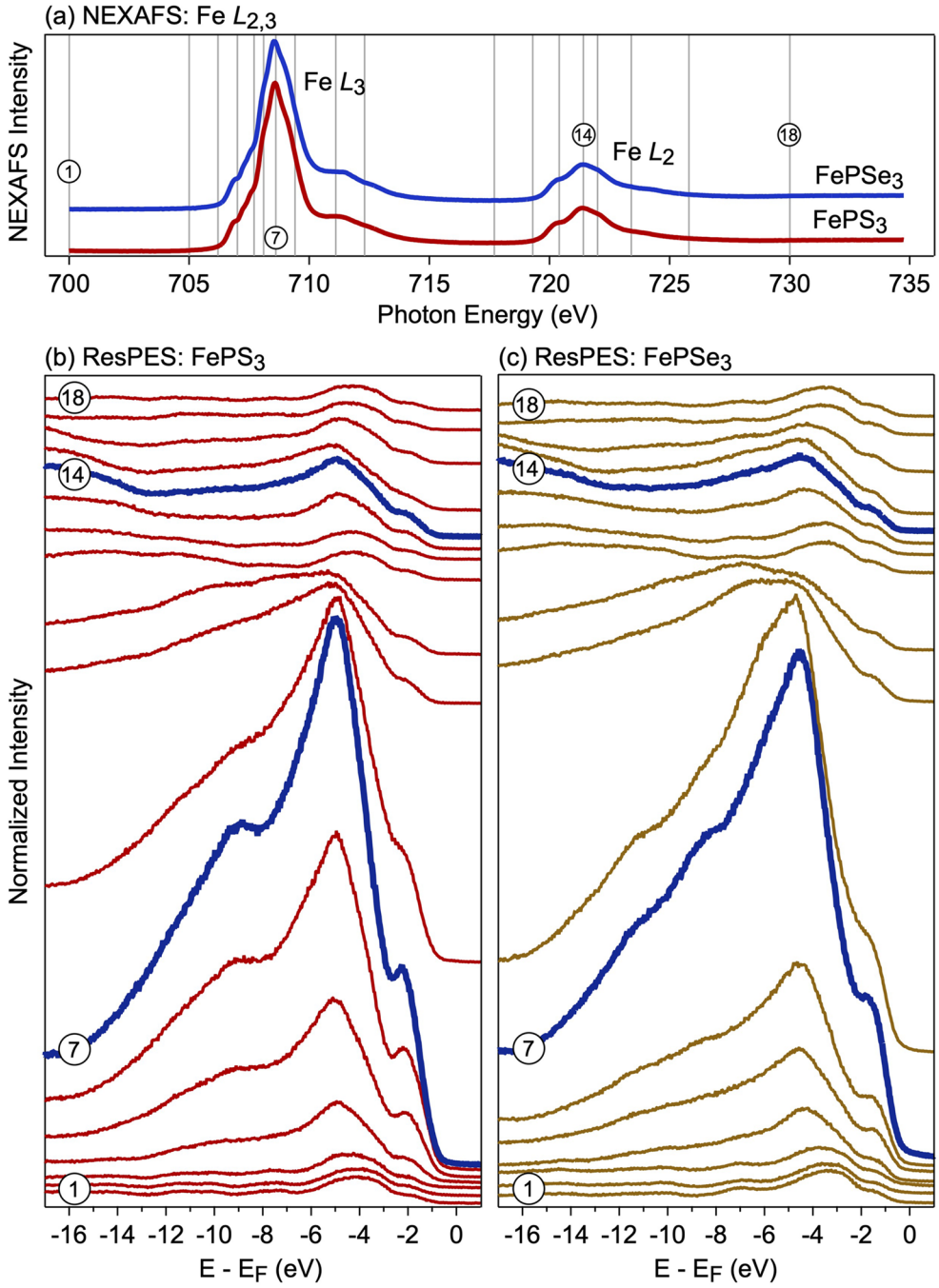

Figure 5. (**a**) The reference Fe $L_{2,3}$ NEXAFS spectra and (**b**,**c**) a series of photoemission spectra taken at the particular photon energies marked by the corresponding vertical line in panel (**a**) for $FePX_3$ crystals. All ResPES spectra are shifted in the vertical direction for clarity. Images are created using Igor Pro (Version 9), https://www.wavemetrics.com.

for the $3d^n\underline{L}$ allowing to assign the measured material to the particular insulator class. Recently, such experiments and analysis of the ResPES data allowed to identify the isostructural layered $NiPS_3$ to the charge transfer insulator state[36]. (Here we have to note that the clear separation between two final states is not possible due to the strong hybridization between them requiring the detailed analysis of the measured resonance photoemission spectra using cluster model calculations).

In Fig. 5b,c the off-resonance spectra of $FePX_3$ collected at $h\nu = 705$ eV demonstrate a broad band in the range of $E - E_F \approx -2.5 \cdots - 6.5$ eV with a shoulder towards E_F (see also Fig. 4d). A set of photoemission satellites is observed at binding energies $E - E_F < -7$ eV. According to our previous theoretical and NEXAFS data, $FePX_3$ are identified as Mott–Hubbard type insulators with $U_{dd} < \Delta$; therefore, the low binding energy structure in the valence band XPS spectra can be assigned to the $3d^{n-1}$ final state structure and the satellite structure to the $3d^n\underline{L}$

final state. The on-resonance spectrum (spectra 7 in Fig. 5b,c) collected at the photon energy of $h\nu = 708.6$ eV (Fe L_3 absorption edge) demonstrates the drastic increase of the photoemission intensity by factor of ≈ 25 in the low binding energy range of $E - E_F \approx 0 \cdots - 6.5$ (with additional shoulders at $E - E_F \approx -8.5$ eV and $E - E_F \approx -10.7$ eV). Taking into account the previous considerations of the ResPES process and that $3d^{n-1}$ Coster-Kronig decay channel dominates the photoemission intensity, we can confirm that the low binding energy resonating structure in the photoemission spectra correspond to the $3d^{n-1}$ final state strongly supporting the description of the $FePX_3$ materials as a Mott–Hubbard type insulator. The similar consideration is also valid for the resonating behavior of the photoemission spectra at the Fe L_2 absorption edge (spectra 14 in Fig. 5b,c). The presented results are in a rather good agreement with the calculated ResPES spectra of FeO (Fe^{2+}) which is also described as a Mott–Hubbard type insulator[58] and with old photoemission data for $FePS_3$[59]. Our results are also supported by the presented DFT calculations for $FePX_3$ (see Fig. 1c,d). As was discussed earlier, the top of the valence band is formed by the hybrid Fe(3*d*)-S(3*p*)/Se(4*p*) states with significant contribution of the Fe-derived states. At the same time the bottom of the conduction band is formed by mainly Fe(3*d*) states, thus confirming the Mott insulator state for $FePX_3$. Also, the more localized nature of the Fe 3*d* valence band states in the vicinity of E_F for $FePS_3$ compared to $FePSe_3$ (see Fig. 1c,d) is experimentally confirmed by the observation of the sharper photoemission intensity of the low binding energy feature at $E - E_F \approx -2.25$ eV for $FePS_3$ (Fig. 5b,c).

Conclusion

In summary, the crystallographic structure and electronic properties of high-quality layered $FePX_3$ (X: S, Se) crystals were studied using different experimental methods including *in situ* UHV surface science techniques, like LEED, NEXAFS, XPS and ResPES in combination with systematic DFT calculations. Our theoretical and spectroscopy results indicate the strong correlation effects in the electronic structure of $FePX_3$ and using NEXAFS, XPS and ResPES methods it is shown that these materials can be described as Mott–Hubbard type insulator with $U_{dd} < \Delta$ according to the Zaanen–Sawatzky–Allen scheme. Particularly, the systematic ResPES experiments performed around the Fe $L_{2,3}$ absorption edge show the strong resonant behavior for the $3d^{n-1}$ final states located at low binding energies in the electronic structure of $FePX_3$. Such behavior is opposite to the case of the isostructural layered $NiPS_3$ materials which was identified as a charge transfer insulator according to the same classification scheme. The present theoretical and spectroscopic results are of a great importance for the fundamental investigations and understanding of the new class of layered materials - transition-metal trichalcogenides, as they provide the clear description of their electronic structure, which is important for further understanding of their transport, optical and catalytic properties. Particularly, it can be important for the understanding of the reaction of $FePX_3$ towards water splitting, where Fe 3*d* states located at the top of the valence band might play a crucial role in this process, bringing these materials as perspective for the low-dimensional oxygen- and hydrogen-gas generation.

Methods

DFT and cluster-based calculations. Spin-polarized DFT calculations based on plane-wave basis sets of 500 eV cutoff energy were performed with the Vienna *ab initio* simulation package (VASP)[60,61]. The Perdew-Burke-Ernzerhof (PBE) exchange-correlation functional[62] was employed. The electron-ion interaction was described within the projector augmented wave (PAW) method[63] with Fe (3*p*, 3*d*, 4*s*), P (3*s*, 3*p*), S (3*s*, 3*p*) and Se (4*s*, 4*p*) states treated as valence states. The Brillouin-zone integration was performed on Γ-centred symmetry reduced Monkhorst-Pack meshes using a Gaussian smearing with $\sigma = 0.05$ eV, except for the calculation of density of states. For these calculations, the tetrahedron method with Blöchl corrections[64] was employed. A $12 \times 12 \times 4$ *k*-mesh was used. The DFT+*U* scheme[65,66] was adopted for the treatment of Fe 3*d* orbitals, with the parameter $U_{\text{eff}} = U - J$ equal to 3 eV. Dispersion interactions were considered adding a $1/r^6$ atom-atom term as parameterized by Grimme ("D2" parameterization)[67]. The spin-orbit interaction is taken into account. The lattice parameters of 3D $FePX_3$ ($a = b$, c, positions of P and S) were fully relaxed for different magnetic states. During structure optimization, the convergence criteria for energy and force were set equal to 10^{-6} eV and $10^{-2}\ eV\ \text{Å}^{-1}$, respectively. The obtained results listed in Table S1 show that both systems under study prefer the AFM state. The respective structures are presented in the Supplementary Information and can be visualized using software VESTA (https://jp-minerals.org/vesta/en/).

The Fe $L_{2,3}$ NEXAFS spectra were calculated using CTM4XAS v5.5 program (https://anorg.chem.uu.nl/CTM4XAS)[68]. The O_h symmetry was considered for simplicity according to the crystallographic structure of the $FePX_3$ single layer where each X=S/Se atom is coordinated with Fe sites.

Samples synthesis and characterization. CVT method was used for the synthesis of $FePX_3$ crystals. Iron (99.9%), phosphorus (99.999%), sulphur (99.999%) and selenium (99.999%) from Shanghai Macklin Biochemical Co., Ltd. and Alfa Aesar were used for synthesis. A stoichiometric amount of high-purity elements (mole ratio Fe : P : X = 1 : 1 : 3, 1 g in total) and iodine (about 20 mg) as a transport agent were sealed into a quartz ampule (length is 15 cm, external diameter is approximately 15 mm) and kept in a two-zone furnace with 700–650 °C and 650–600° C for $FePS_3$ and $FePSe_3$, respectively. The vacuum inside the ampule was pumped down to 1×10^{-3} mbar. After 7 days of heating, the ampule was cooled down to room temperature with bulk crystals in the colder edge.

After synthesis, the systematic characterization of samples was performed: (1) optical images were obtained with optical microscope at different magnifications; (2) XRD patterns were collected at room temperature with a Bruker D2 Phaser diffractometer using Cu K (1.54178 Å) radiation; (3) for the Raman characterization, a Nanofinder 30 was used to obtain high-resolution spectra. The $FePX_3$ samples were illuminated with a laser wavelength of 532 nm and power 32 mW with a 1 μm laser spot. Before characterization, standard single-crystal

silicon was used to calibrate the system. For measurements, an integration time (the exposure time) of 5 s and an accumulation of 3 were set to obtain spectra with high signal-to-noise ratio; (4) TEM measurements were performed using FEI Tecnai G2 F30 instrument and the focused ion beam preparation was performed using FEI Strata 400S; (5) SEM/EDX data were collected using ZEISS SIGMA 500 microscope; (6) LEED measurements were performed in ultra-high vacuum (UHV) conditions using MCP-LEED (Scienta Omicron) with the electron beam current of 50–200 pA.

PES and NEXAFS experiments. All photoelectron spectroscopy measurements were performed at the Russian-German dipole soft X-ray beamline (RGBL-dipole) of the BESSY II synchrotron radiation facility (Helmholtz-Zentrum Berlin)[69]. All spectra were measured in UHV conditions (vacuum is below than 2×10^{-10} mbar) and at room temperature. Before every set of experiments, new sample was cleaved in air and immediately introduced in vacuum, followed by the degassing routine at 350°C for 60 min. NEXAFS spectra were collected in the total electron yield (TEY) mode using sample drain current. XPS core-level and ResPES valence band spectra were acquired using SPECS PHOIBOS 150 analyser. Photon energies in all experiments were calibrated using a polycrystalline Au sample. During ResPES measurements the effect of a sample charging was minimal (within 1 eV) and was not compensated; however, the correctness of every measurement was confirmed by the acquisition of the respective S 2*p* or Se 3*p* spectra at every photon energy step before and after collection of the corresponding valence band spectra.

Received: 11 November 2021; Accepted: 22 December 2021
Published online: 14 January 2022

References

1. Ludwig, A. Discovery of new materials using combinatorial synthesis and high-throughput characterization of thin-film materials libraries combined with computational methods. *NPJ Comput. Mater.* **5**, 70 (2019).
2. Wellmann, P. J. The search for new materials and the role of novel processing routes. *Discov. Mater.* **1**, 14 (2021).
3. Kumar, P. *et al.* Review: Two-dimensional layered materials for energy storage applications. *ECS J. Solid State Sci. Technol.* **5**, Q3021–Q3025 (2016).
4. Zhan, H., Guo, D. & Xie, G. Two-dimensional layered materials: from mechanical and coupling properties towards applications in electronics. *Nanoscale* **11**, 13181–13212 (2019).
5. Gutierrez, H. R. Two-dimensional layered materials offering expanded applications in flatland. *ACS Appl. Nano Mater.* **3**, 6134–6139 (2020).
6. Kulyk, B. *et al.* A critical review on the production and application of graphene and graphene-based materials in anti-corrosion coatings. *Crit. Rev. Solid State Mater. Sci.* 1–48 (2021).
7. Wang, T. *et al.* A review on graphene-based gas/vapor sensors with unique properties and potential applications. *Nanomicro Lett.* **8**, 95–119 (2016).
8. Larki, F., Abdi, Y., Kameli, P. & Salamati, H. An effort towards full graphene photodetectors. *Photonic Sens.* 1–37 (2020).
9. Tkachev, S. *et al.* Environmentally friendly graphene inks for touch screen sensors. *Adv. Funct. Mater.* **31**, 2103287 (2021).
10. Peplow, M. Graphene booms in factories but lacks a killer app. *Nature* **522**, 268–269 (2015).
11. Park, S. The puzzle of graphene commercialization. *Nat. Rev. Mater.* **1**, 16085 (2016).
12. Xu, W. & Lee, T.-W. Recent progress in fabrication techniques of graphene nanoribbons. *Mater. Horiz.* **3**, 186–207 (2016).
13. Liu, C. *et al.* Highly stretchable graphene nanoribbon springs by programmable nanowire lithography. *NPJ 2D Mater. Appl.* **3**, 23 (2019).
14. Yu, W., Sisi, L., Haiyan, Y. & Jie, L. Progress in the functional modification of graphene/graphene oxide: A review. *RSC Adv.* **10**, 15328–15345 (2020).
15. Nurazzi, N. M. *et al.* The frontiers of functionalized graphene-based nanocomposites as chemical sensors. *Nanotechnol. Rev.* **10**, 330–369 (2021).
16. Manzeli, S., Ovchinnikov, D., Pasquier, D., Yazyev, O. V. & Kis, A. 2D transition metal dichalcogenides. *Nat. Rev. Mater.* **2**, 17033 (2017).
17. Gogotsi, Y. & Anasori, B. The rise of MXenes. *ACS Nano* **13**, 8491–8494 (2019).
18. Du, C.-F. *et al.* Layered trichalcogenidophosphate: A new catalyst family for water splitting. *Nanomicro Lett.* **10**, 67 (2018).
19. Wang, F. *et al.* New frontiers on van der Waals layered metal phosphorous trichalcogenides. *Adv. Funct. Mater.* **28**, 1802151 (2018).
20. Samal, R., Sanyal, G., Chakraborty, B. & Rout, C. S. Two-dimensional transition metal phosphorous trichalcogenides (MPX_3): A review on emerging trends, current state and future perspectives. *J. Mater. Chem. A* **9**, 2560–2591 (2020).
21. Du, K.-Z. *et al.* Weak van der Waals stacking, wide-range band gap, and Raman study on ultrathin layers of metal phosphorus trichalcogenides. *ACS Nano* **10**, 1738–1743 (2016).
22. Zhang, X., Zhao, X., Wu, D., Jing, Y. & Zhou, Z. $MnPSe_3$ monolayer: A promising 2D visible-light photohydrolytic catalyst with high carrier mobility. *Adv. Sci.* **3**, 1600062 (2016).
23. Yang, J., Zhou, Y., Guo, Q., Dedkov, Y. & Voloshina, E. Electronic, magnetic and optical properties of $MnPX_3$ (X = S, Se) monolayers with and without chalcogen defects: A first-principles study. *RSC Adv.* **10**, 851–864 (2020).
24. Li, X. *et al.* High-yield electrochemical production of large-sized and thinly layered $NiPS_3$ flakes for overall water splitting. *Small* **15**, 1902427 (2019).
25. Li, X., Cao, T., Niu, Q., Shi, J. & Feng, J. Coupling the valley degree of freedom to antiferromagnetic order. *Proc. Natl. Acad. Sci. U.S.A.* **110**, 3738–3742 (2013).
26. Li, X., Wu, X. & Yang, J. Half-metallicity in $MnPSe_3$ exfoliated nanosheet with carrier doping. *J. Am. Chem. Soc.* **136**, 11065–11069 (2014).
27. Zhong, L., Chen, X. & Qi, J. Controlling the spin and valley degeneracy splitting in monolayer $MnPSe_3$ by atom doping. *Phys. Chem. Chem. Phys.* **19**, 15388–15393 (2017).
28. Pei, Q., Song, Y., Wang, X., Zou, J. & Mi, W. Superior electronic structure in two-dimensional $MnPSe_3/MoS_2$ van der Waals heterostructures. *Sci. Rep.* **7**, 9504 (2017).
29. Pei, Q. & Mi, W. Electrical control of magnetic behavior and valley polarization of monolayer antiferromagnetic $MnPSe_3$ on an insulating ferroelectric substrate from first principles. *Phys. Rev. Appl.* **11**, 014011 (2019).

30. Zhang, X.-X. *et al.* Spin dynamics slowdown near the antiferromagnetic critical point in atomically thin $FePS_3$. *Nano Lett.* **21**, 5045–5052 (2021).
31. Zhang, Q. *et al.* Observation of giant optical linear dichroism in a zigzag antiferromagnet $FePS_3$. *Nano Lett.* **21**, 6938–6945 (2021).
32. Mukherjee, D., P, M. A. & Sampath, S. Few-layer iron selenophosphate, $FePSe_3$: Efficient electrocatalyst toward water splitting and oxygen reduction reactions. *ACS Appl. Energy Mater.* **1**, 220–231 (2017).
33. Sandhya, K. S. & Suresh, C. H. Water splitting promoted by a ruthenium(II) PNN complex: An alternate pathway through a dihydrogen complex for hydrogen production. *Organometallics* **30**, 3888–3891 (2011).
34. Xue, L.-X., Meng, T.-T., Yang, W. & Wang, K.-Z. Recent advances in ruthenium complex-based light-driven water oxidation catalysts. *J. Photochem. Photobiol. B, Biol.* **152**, 95–105 (2015).
35. Kamdar, J. M. & Grotjahn, D. B. An overview of significant achievements in ruthenium-based molecular water oxidation catalysis. *Molecules* **24**, 494 (2019).
36. Yan, M. *et al.* Correlations in the electronic structure of van der Waals $NiPS_3$ crystals: An x-ray absorption and resonant photoelectron spectroscopy study. *J. Phys. Chem. Lett.* **12**, 2400–2405 (2021).
37. Sen, P. & Chouhan, R. K. Electronic structure of MPX_3 trichalcogenide monolayers in density functional theory: A case study with four compounds (M = Mn, Fe; X = S, Se). *Electron. Struct.* **2**, 025003 (2020).
38. Zaanen, J., Sawatzky, G. A. & Allen, J. W. Band gaps and electronic structure of transition-metal compounds. *Phys. Rev. Lett.* **55**, 418–421 (1985).
39. Xie, Q.-Y. *et al.* Crystallographic and magnetic properties of van der Waals layered $FePS_3$ crystal. *Chin. Phys. B* **28**, 056102 (2019).
40. Wang, X. *et al.* Raman spectroscopy of atomically thin two-dimensional magnetic iron phosphorus trisulfide ($FePS_3$) crystals. *2D Mater.* **3**, 031009 (2016).
41. Mukherjee, D., Austeria, P. M. & Sampath, S. Two-dimensional, few-layer phosphochalcogenide, $FePS_3$: A new catalyst for electrochemical hydrogen evolution over wide pH range. *ACS Energy Lett.* **1**, 367–372 (2016).
42. Gota, S., Guiot, E., Henriot, M. & Gautier-Soyer, M. Atomic-oxygen-assisted MBE growth of α-Fe_2 O_3 on α-Al_2 O_3(0001): Metastable FeO(111)-like phase at subnanometer thicknesses. *Phys. Rev. B* **60**, 14387–14395 (1999).
43. Yamashita, T. & Hayes, P. Analysis of XPS spectra of Fe^{2+} and Fe^{3+} ions in oxide materials. *Appl. Surf. Sci.* **254**, 2441–2449 (2008).
44. Miedema, P. S. & Groot, F. M. d. The iron L edges: Fe 2p X-ray absorption and electron energy loss spectroscopy. *J. Electron Spectrosc. Relat. Phenom.* **187**, 32–48 (2013).
45. Ahmed, F., Kumar, S., Arshi, N., Anwar, M. S. & Koo, B. H. Morphological evolution between nanorods to nanosheets and room temperature ferromagnetism of Fe-doped ZnO nanostructures. *CrystEngComm* **14**, 4016–4026 (2012).
46. Liu, J. *et al.* Predication of screened hybrid functional on transition metal monoxides: From Mott insulator to charge transfer insulator. *J. Alloys Compd.* **808**, 151707 (2019).
47. Yang, S. *et al.* Soft X-ray XANES studies of various phases related to $LiFePO_4$ based cathode materials. *Energy Environ. Sci.* **5**, 7007–7016 (2012).
48. Farrell, S. P. *et al.* Evolution of local electronic structure in alabandite and niningerite solid solutions [(Mn, Fe)S, (Mg, Mn)S, (Mg, Fe)S] using sulfur K- and L-edge XANES spectroscopy. *Am. Mineral.* **87**, 1321–1332 (2002).
49. Kruse, J. *et al.* Phosphorus $L_{2,3}$-edge XANES: overview of reference compounds. *J. Synchrotron Radiat.* **16**, 247–259 (2009).
50. Davis, L. C. & Feldkamp, L. A. Resonant photoemission involving super-Coster-Kronig transitions. *Phys. Rev. B* **23**, 6239 (1981).
51. Davis, L. C. Theory of resonant photoemission spectra of 3d transition-metal oxides and halides. *Phys. Rev. B* **25**, 2912–2915 (1982).
52. Solomon, E. I., Basumallick, L., Chen, P. & Kennepohl, P. Variable energy photoelectron spectroscopy: electronic structure and electronic relaxation. *Coord. Chem. Rev.* **249**, 229–253 (2005).
53. Fujimori, A. Electronic structure of MnO. *Phys. Rev. B* **42**, 7580–7586 (1990).
54. Okada, K., Kotani, A. & Thole, B. Charge transfer satellites and multiplet splitting in X-ray photoemission spectra of late transition metal halides. *Electron Spectrosc. Relat. Phenom.* **58**, 325–343 (1992).
55. Tjernberg, O. *et al.* Resonant photoelectron spectroscopy on NiO. *Phys. Rev. B* **53**, 10372–10376 (1996).
56. Nesbitt, H. W., Legrand, D. & Bancroft, G. M. Interpretation of Ni 2p XPS spectra of Ni conductors and Ni insulators. *Phys. Chem. Miner.* **27**, 357–366 (2000).
57. Taguchi, M. *et al.* Revisiting the valence-band and core-level photoemission spectra of NiO. *Phys. Rev. Lett.* **100**, 206401 (2007).
58. Tanaka, A. & Jo, T. Resonant 3d, 3p and 3s photoemission in transition metal oxides predicted at 2p threshold. *J. Phys. Soc. Jpn.* **63**, 2788–2807 (1994).
59. Kamata, A. *et al.* Resonant 2p → 3d photoemission measurement of MPS_3 (M=Mn, Fe, Ni). *J. Phys. Soc. Jpn.* **66**, 401–407 (1997).
60. Kresse, G. & Hafner, J. Norm-conserving and ultrasoft pseudopotentials for first-row and transition elements. *J. Phys.: Condens. Matter* **6**, 8245 (1994).
61. Kresse, G. Efficient iterative schemes for ab initio total-energy calculations using a plane-wave basis set. *Phys. Rev. B* **54**, 11169–11186 (1996).
62. Perdew, J. P., Burke, K. & Ernzerhof, M. Generalized gradient approximation made simple. *Phys. Rev. Lett.* **77**, 3865–3868 (1996).
63. Blöchl, P. E. Projector augmented-wave method. *Phys. Rev. B* **50**, 17953–17979 (1994).
64. Blöchl, P. E., Jepsen, O. & Andersen, O. K. Improved tetrahedron method for Brillouin-zone integrations. *Phys. Rev. B* **49**, 16223–16233 (1994).
65. Anisimov, V. I., Aryasetiawan, F. & Lichtenstein, A. I. First-principles calculations of the electronic structure and spectra of strongly correlated systems: the LDA+ U method. *J. Phys.: Condens. Matter* **9**, 767 (1997).
66. Dudarev, S. L. Electron-energy-loss spectra and the structural stability of nickel oxide: An LSDA+U study. *Phys. Rev. B* **57**, 1505–1509 (1998).
67. Grimme, S. Semiempirical GGA-type density functional constructed with a long-range dispersion correction. *J. Comput. Chem.* **27**, 1787–1799 (2006).
68. Stavitski, E. & Groot, F. M. d. The CTM4XAS program for EELS and XAS spectral shape analysis of transition metal L edges. *Micron* **41**, 687–694 (2010).
69. Molodtsov, S. L. *et al.* High-resolution Russian-German beamline at BESSY. *Appl. Phys. A* **94**, 501–505 (2009).

Acknowledgements

We would like to acknowledge Anna Makarova and Dmitry Smirnov for their technical support during beamtime at HZB. Y.D. and E.V. thank the "ENSEMBLE3 - Centre of Excellence for nanophotonics, advanced materials and novel crystal growth-based technologies" project (GA No. MAB/2020/14) carried out within the International Research Agendas programme of the Foundation for Polish Science co-financed by the European Union under the European Regional Development Fund and the European Union's Horizon 2020 research and innovation programme Teaming for Excellence (GA. No. 857543) for support of this work. We thank HZB for the allocation of synchrotron radiation beamtime and for support within the bilateral Russian-German Laboratory program. The North-German Supercomputing Alliance (HLRN) is acknowledged for providing computer time.

Author contributions

Y.D. and E.V. proposed the study. Y.J. and M. Y. performed synthesis and characterization of the samples. T.K. and Y.D. performed PES and NEXAFS experiments. E.V. performed DFT calculations. All authors contribute in the analysis of data and writing of manuscript.

Funding

Open Access funding enabled and organized by Projekt DEAL.

Competing interests

The authors declare no competing interests.

Additional information

Supplementary Information The online version contains supplementary material available at https://doi.org/10.1038/s41598-021-04557-1.

Correspondence and requests for materials should be addressed to E.V. or Y.D.

Reprints and permissions information is available at www.nature.com/reprints.

Publisher's note Springer Nature remains neutral with regard to jurisdictional claims in published maps and institutional affiliations.